

Superconductivity in 122-type antimonide BaPt₂Sb₂

Motoharu Imai¹, Soshi Ibuka^{1*}, Naoki Kikugawa¹, Taichi Terashima², Shinya Uji², Takeshi Yajima^{3,4}, Hiroshi Kageyama³, and Izumi Hase⁵

¹ Superconducting Property Unit, National Institute for Materials Science, 1-2-1 Sengen, Tsukuba, Ibaraki 305-0048, Japan.

² Superconducting Property Unit, National Institute for Materials Science, 3-13 Sakura, Tsukuba, Ibaraki 305-0003, Japan.

³ Graduate School of Engineering, Kyoto University, Nishikyo-ku, Kyoto 615-8510, Japan

⁴ Institute for Solid State Physics, University of Tokyo, 5-1-5 Kashiwanoha, Kashiwa, Chiba 277-85851, Japan.

⁵ Electronics and Photonics Research Institute, National Institute of Advanced Industrial Science and Technology, AIST Central 2, 1-1-4 Umezono, Tsukuba, Ibaraki 305-8568, Japan.

* Present address: Institute of Materials Structure Science, High Energy Accelerator Research Organization, 203-1 Shirakata, Tokai, Ibaraki 319-1106, Japan

The crystal structure, superconducting properties, and electronic structure of a novel superconducting 122-type antimonide, BaPt₂Sb₂, have been investigated by measurements of powder X-ray diffraction patterns, electrical resistivity, ac magnetic susceptibility, specific heat as well as ab-initio calculations. This material crystallizes in a new-type of monoclinic variant of the CaBe₂Ge₂-type structure, in which Pt₂Sb₂ layers consisting of PtSb₄ tetrahedra and Sb₂Pt₂ layers consisting of SbPt₄ tetrahedra are stacked alternatively and Ba atoms are located between the layers. Measurements of electrical resistivity, ac magnetic susceptibility and specific heat revealed that BaPt₂Sb₂ is a superconducting material with a T_C of 1.8 K. The electronic heat capacity coefficient γ_n and Debye temperature θ_D were 8.6(2) mJ/mol K² and 146(4) K, where the figures in parentheses represent the standard deviation. The upper critical field $\mu_0 H_{C2}(0)$ and the Ginzburg-Landau coherent length $\xi(0)$ were determined to be 0.27 T and 35 nm. Calculations showed that it has two three-dimensional Fermi surfaces (FSs) and two two-dimensional FSs, leading to anisotropic transport properties. The d-states of the Pt atoms in the Pt₂Sb₂ layers mainly contribute to $N(E_F)$. A comparison between experimental and calculated results indicates that BaPt₂Sb₂ is a superconducting material with moderate coupling.

PACS: 74.70.Xa, 74.25.-q, 74.20.Pq

I. INTRODUCTION

The discovery of superconductivity with a critical temperature T_C of 26 K in $\text{LaFeAs}(\text{O},\text{F})$ ¹ stimulated studies on superconducting iron pnictides. Consequently, various types of superconducting iron pnictides, such as 1111, 122, 11 systems have been discovered.²⁻⁹ AFe_2As_2 ($A = \text{Ba}, \text{Sr}, \text{Ca}, \text{or Eu}$) is the parent material of superconducting 122 iron pnictides. Partial substitution of A , Fe , or As or pressurization induce superconductivity with a relatively high T_C . For example, $(\text{Ba},\text{K})\text{Fe}_2\text{As}_2$ and $(\text{Ca}, \text{La})\text{Fe}_2(\text{As}, \text{P})_2$ have T_C of 38 K and 45 K, respectively.^{10, 11} AFe_2As_2 crystallizes in the ThCr_2Si_2 -type structure, in which A atoms are located between Fe_2As_2 layers. The Fe_2As_2 layer is composed of an Fe square lattice, where each Fe atom is surrounded by four As atoms in tetrahedral coordination.

Superconductivity has also been observed in iron-free pnictides with the ThCr_2Si_2 -type or related structure, although their T_C values are relatively low.¹²⁻¹⁹ SrPt_2As_2 is a superconductor with a T_C of 5.4 K.²⁰ It crystallizes in a modulated orthorhombic variant of the CaBe_2Ge_2 -type structure, a derivative structure of the ThCr_2Si_2 -type.²¹ In SrPt_2As_2 with the CaBe_2Ge_2 -type structure (referred to hereafter as CaBe_2Ge_2 -type SrPt_2As_2), Sr atoms are sandwiched by two kinds of layers. One is a Pt_2As_2 layer, which is the same as that in AFe_2As_2 . The other is an As_2Pt_2 layer, in which As atoms form a square lattice and each As atom is surrounded by four Pt atoms in tetrahedral coordination. The electronic structure has been calculated for ThCr_2Si_2 -type SrPt_2As_2 (SrPt_2As_2 with the ThCr_2Si_2 -type structure), which is a hypothetical material, as well as CaBe_2Ge_2 -type SrPt_2As_2 .²² The calculations show that the Fermi surfaces (FSs) of the CaBe_2Ge_2 -type SrPt_2As_2 have intermediate character between AFe_2As_2 and ThCr_2Si_2 -type iron-free pnictides. AFe_2As_2 has two-dimensional (2D) FSs^{2,3,5,6,23,24} while ThCr_2Si_2 -type iron-free pnictides have three-dimensional (3D) FSs.²⁵⁻²⁹ The CaBe_2Ge_2 -type SrPt_2As_2 has two 2D-like FSs and two 3D-like ones. The coexistence of 2D and 3D FS has also been reported in CaBe_2Ge_2 -type BaPd_2Sb_2 .²⁹ Thus, some of the CaBe_2Ge_2 -type iron-free pnictides are positioned between the ThCr_2Si_2 -type iron pnictides and the ThCr_2Si_2 -type iron-free pnictides from the view-point of the Fermi surfaceology. Therefore, the study of superconductivity in the CaBe_2Ge_2 -type pnictides is significant for a better and systematic understanding of superconductivity in 122 pnictides.

Superconducting materials structurally related to the iron-based superconducting materials have thus far been limited to phosphides and arsenides. Recently, a 122 antimonide, SrPt_2Sb_2 , has been reported to be a superconductor with a T_C of 2.1 K.³⁰ This is the first reported superconducting 122 antimonide that is related to superconducting iron pnictides, to the best of our knowledge. The crystal structure of SrPt_2Sb_2 is different from that of CaBe_2Ge_2 -type, which was reported previously.²¹ Although a precise analysis of the crystal structure needs to be carried out, it is plausibly related to the CaBe_2Ge_2 -type structure. Since SrPt_2Sb_2 is isovalent to SrPt_2As_2 and has a crystal structure related to the CaBe_2Ge_2 -type, SrPt_2Sb_2 is expected to have both 3D and 2D FSs and

to show physical properties that reflects this.

In this paper, we report on the successful synthesis of BaPt_2Sb_2 , its crystal and electronic structures, and the appearance of superconductivity in the material. BaPt_2Sb_2 is a novel material to the best of our knowledge. Powder X-ray diffractometry indicates that it crystallizes in a monoclinic variant of the CaBe_2Ge_2 -type structure. Measurements of electrical resistivity, ac magnetic susceptibility, and specific heat reveal that BaPt_2Sb_2 is a superconducting material with a T_C of 1.82 K. Ab-initio calculations demonstrate that it has 3D and 2D FSs and the Pt-d states largely contribute to $N(E_F)$, which is responsible for its superconductivity.

II. EXPERIMENTAL METHODS

The starting materials used are Ba (99.9% purity), Pt (99.95% purity), and Sb (99.999% purity). Samples were synthesized by Ar-arc melting of a 1.05:2:2 molar mixture of Ba, Pt, and Sb. Electron micro-probe analysis (EPMA) revealed that the sample consisted of a matrix with chemical composition of 20.2 at.% Ba, 40.6 at.% Pt, and 39.3 at.% Sb, and a small amount of precipitates of Pt_xSb .

The crystal structure was examined by powder X-ray diffractometry. The X-ray diffraction (XRD) measurements were performed on a Bragg-Brentano diffractometer RINT-TTR III (Rigaku) using Cu $K\alpha$ radiation (40 kV, 300 mA) with a step width of 0.02° in the 2θ range of $15.0\text{--}120.0^\circ$ at room temperature. For the measurements, a fine powder sample was mounted on a glass plate holder of 0.3 mm depth. The observed XRD pattern was analyzed by the direct-space method with simulated annealing algorithm and subsequently refined by the Rietveld method³¹ using the software "FullProf".³² The background was modeled as a six-coefficient polynomial function.

The electrical resistivity ρ at temperatures ranging from 1.8 to 300.0 K was measured by a four-probe method using a physical properties measurement system (PPMS, Quantum Design Co.). The magnetic field dependence of ρ was measured using a standard ac technique with a frequency (f) of ~ 15 Hz.

We measured the ac susceptibility $\chi_{ac} = \chi' - i\chi''$ by a mutual-inductance method with an ac modulation field of $(\mu_0 H_{ac}) \sim 0.037$ mT and $f \sim 67$ Hz. For this, we used the same sample that was used for the ac resistivity measurements. The sample was cooled down with a dilution fridge that was equipped with a superconducting magnet to apply the external fields. The specific heat was measured by a relaxation method using PPMS.

In order to investigate the electronic structure of BaPt_2Sb_2 , we performed an *ab-initio* band calculation for this compound. We used the full-potential augmented plane-wave (FLAPW) scheme and the exchange-correlation potential was constructed within the local-density approximation (LDA). These are implemented as KANSAI-94 and TSPACE³³ computer codes. The space group is C2/m (No. 12), and the lattice constants and atomic parameters were fixed at the experimentally

observed ones obtained in this work. Muffin-tin radii used in this calculation are 2.6 bohr for Ba, 2.4 bohr for Pt and 2.3 bohr for Sb, respectively. For the plane wave basis functions, we used about 1000 LAPWs. Since this compound contains the heavy atoms Pt and Sb, we included the spin-orbit interaction (SOI) in the second-variational approach.³⁴ In this scheme, we first perform the scalar-relativistic calculation, and then include SOI iteratively.

III. RESULTS AND DISCUSSION

A. Crystal Structure

Figure 1 shows a powder XRD pattern of BaPt₂Sb₂ together with the results of Rietveld analysis. The observed pattern can be reproduced well assuming that BaPt₂Sb₂ has a monoclinic structure with the parameters shown in Table I and that a small amount (0.8 mol %) of impurity phase PtSb is mixed. Figure 2 illustrates the crystal structure of BaPt₂Sb₂. The blue solid lines represent a unit cell. The crystal structure of BaPt₂Sb₂ is a new monoclinic variant of the CaBe₂Ge₂-type. In this structure, the Pt1 and Sb2 atoms form the Pt₂Sb₂ layers that consist of PtSb₄ tetrahedra, while the Pt2 and Sb1 atoms form the Sb₂Pt₂ layers that consist of SbPt₄ tetrahedra, and these layers are stacked alternately along the [001] direction with Ba atoms located between the layers. These feature is the same as those of the CaBe₂Ge₂-type. The following features are different from the CaBe₂Ge₂-type. First, the angle between the *c*-axis and the *a*-*b* plane, β_{uc} , is 91.227°, while the three angles α_{uc} , β_{uc} , and γ_{uc} , are 90.00° in the CaBe₂Ge₂-type (Fig. 2 (d)). Second, the Pt1 (or Sb1) atoms form a deformed square lattice in the Pt₂Sb₂ (or Sb₂Pt₂) layers in the proposed structure while Pt (or Sb) atoms form a square lattice in the Pt₂Sb₂ (or Sb₂Pt₂) layers in the CaBe₂Ge₂-type BaPt₂Sb₂ (hypothetical) as shown in Figs. 2(e) and 2(f). The shape of the lattice formed by Pt1 (or Sb1) atoms is an isosceles trapezoid, and the degree of deformation in the Pt1 lattice is larger than that of the Sb1 lattice. Pt1 (or Sb1) atoms are arranged in a line in the *b*-axis direction while they are arranged in a zigzag fashion in the *a*-axis direction. Third, the Pt1 (or Sb1) deformed square lattice in the proposed structure is almost parallel to the *a*- and *b*-axis while the square lattice in the CaBe₂Ge₂-type rotates 45° with respect to the *a*- and *b*-axis (Figs. 2(e) and 2(f), respectively).

A monoclinic variant of the CaBe₂Ge₂-type has been reported in materials such as LnPt₂Ge₂ (Ln = La-Dy),³⁵ and a high-pressure phase of SrPt₂As₂,²¹ which is known as the LaPt₂Ge₂-type structure. The LaPt₂Ge₂-type structure can be obtained from the CaBe₂Ge₂-type by changing the *b*-axis length and increasing the unit-cell angle β from 90° by several tenths of a degree. The relation between the unit cell axis and the square Pt lattice is different between the LaPt₂Ge₂-type and the proposed crystal structure of BaPt₂Sb₂; in the LaPt₂Ge₂-type, the square lattice rotates 45° with respect to the *a* and *b* axis as in the case of the CaBe₂Ge₂-type, while the square lattice is almost parallel to the *a* and *b* axis in BaPt₂Sb₂. Thus, this proposed structure is a novel one to the best of our knowledge.

Table II lists the interatomic distances. The intralayer interatomic distance has two values, 2.681(3) and 2.734(3) Å. The interlayer interatomic distance (2.708(7) Å) is almost the same as the intralayer interatomic distances. In this meaning, the crystal structure is three dimensional. The T_C of iron-based superconductors has often been discussed with two structural parameters, the Pn-Fe-Pn angle in the FePn₄ tetrahedron and the Pn height from the Fe square lattice, where Pn represents pnictogen.³⁶⁻³⁸ The Sb-Pt-Sb angles in the PtSb₄ tetrahedron and the Pt-Sb-Pt angles in the SbPt₄ tetrahedron are far from the ideal regular tetrahedron angle of 109.5° that is thought to be favorable for high T_C in the iron pnictides. The Sb height from the distorted Pt square lattice is in the range of the Pn height of the iron pnictides with high T_C .

The crystal structure of SrPt₂Sb₂ is reported to be different from the CaBe₂Ge₂-type,³⁰ contrary to the claim by Imre et al.,²¹ and it has not been determined yet. The structure proposed in the present work may be helpful to clarify the crystal structure of SrPt₂Sb₂.

B. Electrical Resistivity, ac magnetic susceptibility, specific heat, and magnetic phase diagram

We found that BaPt₂Sb₂ undergoes a superconducting transition based on the results of the measurements of electrical resistivity, ac magnetic susceptibility, and specific heat.

Figure 3(a) shows the electrical resistivity ρ as a function of temperature, and the inset shows an extended view at low temperatures. ρ decreases with decreasing temperature; it shows an abrupt decrease at 1.85 K and it becomes negligibly small at 1.82 K, which suggests that BaPt₂Sb₂ undergoes a normal-to-superconducting transition. The residual resistivity ratio RRR [$\rho(300\text{ K})/\rho(2\text{ K})$] is 4.04. Figure 3(b) shows ρ measured at constant temperatures as a function of the magnetic field. When a magnetic field was applied, the sample underwent a superconducting-to-normal transition. The symbols $H_{C2}^{\rho\text{-on}}$, $H_{C2}^{\rho\text{-mid}}$, $H_{C2}^{\rho\text{-comp}}$ represent the magnetic field at which ρ starts to increase from zero resistivity, the value of ρ at half of the normal resistivity value, and an extrapolation of the ρ - T curve at the transition reaching the normal resistivity value, respectively. The critical field increases with decreasing temperature. The details are discussed later.

Figure 4 shows the real and imaginary part of the ac magnetic susceptibility, χ' and χ'' , measured at constant temperatures below 1.44 K as a function of magnetic field amplitude $\mu_0 H$. The inset shows an expanded view of χ' measured at 0.03K. χ' shows a diamagnetic signal at low $\mu_0 H$ and the diamagnetic signal disappears at $\mu_0 H_{C2}^{\chi'}$ with increasing $\mu_0 H$. χ'' shows a peak at the magnetic field amplitude nearly equal to the inflection point of the $\mu_0 H - \chi'$ curve. The shoulder observed at low $\mu_0 H$ in the $\mu_0 H - \chi''$ curve is a background signal that comes from the apparatus. This behavior of χ' and χ'' suggests that BaPt₂Sb₂ undergoes a superconducting transition in this temperature range,³⁹ and that the abrupt decrease of ρ at 1.85 K corresponds to a superconducting transition. The magnitude of the diamagnetic signal of BaPt₂Sb₂ in χ' was investigated by comparing it with the diamagnetic signal of Pb with the same shape and size. Since the magnitude of the

observed diamagnetic signal of BaPt₂Sb₂ is almost the same as that of Pb measured at 1.6 K, at which the Pb sample is a perfect diamagnet, the volume fraction of superconductivity is approximately 100 % in BaPt₂Sb₂.

Figure 5(a) shows the specific heat divided by the temperature, C/T , measured at various magnetic fields as a function of the temperature squared, T^2 . C/T has an anomaly around 1.7 K for 0 T. This anomaly shifts to a lower temperature and becomes smaller with increasing magnetic field strength and it disappears at 0.2 T. The large specific heat anomaly and the large diamagnetic signal in χ' indicate that the observed superconductivity is bulk superconductivity. These results reveal that BaPt₂Sb₂ is a superconducting material with T_C of 1.8 K.

We determined the electronic specific heat coefficient γ_n , the coefficients β and δ to be 8.6(2) mJ/mol K², 2.32(6) mJ/mol K⁴, and 0.111(5) mJ/mol K⁶, respectively, by fitting the data obtained at 0.2 T into the equation $C/T = \gamma_n + \beta T^2 + \delta T^4$, where the figures in parentheses represent the standard deviation. The Debye temperature θ_D was calculated to be 146(4) K, from the value of β . In order to confirm the validity of the fitting, we calculated the difference in entropy between the normal and superconducting states, $S_{es} - S_{en}$, by integrating $(C_{es} - \gamma_n)/T$ between 0 and 2 K, where C_{es} is the electronic specific heat of the superconducting state. C_{es} is obtained by subtracting the phonon specific heat $C_{ph} = \beta T^3 + \delta T^5$ from $C(0\text{ T})$ and extrapolating $C_{es}(0\text{ T})$ to 0 K. The entropy difference goes to zero, when the temperature reaches 1.8 K, as shown in the inset, which confirms the thermodynamic consistency of the fitting.

In Fig. 5(b), the difference in C/T between 0 T and 0.2 T, $[C(0\text{ T}) - C(0.2\text{ T})]/T$, is shown as a function of the temperature. The dashed line represents an entropy-conserving construction. The transition to the superconducting state with an entropy-conserving construction gives $\Delta C(T_C)/T_C = 11.8(2)$ mJ/molK² and $T_C = 1.66$ K. The ratio of the specific heat jump at T_C to γ_n , $\Delta C(T_C)/\gamma_n T_C$, is calculated to be 1.37, which is almost the same as the value of the BCS theory of 1.43.⁴⁰

The anomaly in the C/T - T curve has a shoulder at 1.76 K. A detailed investigation of the shoulder is underway, although one plausible origin is spatial inhomogeneity of the chemical composition in the samples.

Figure 6(a) shows a magnetic field-temperature diagram deduced from the measurements of electrical resistivity, ac magnetic susceptibility, and specific heat. The open triangle, circle and rhombus symbols indicate $T_C^{\rho\text{-on}}$, $T_C^{\rho\text{-mid}}$, and $T_C^{\rho\text{-comp}}$ shown in Fig 3(b), respectively. The solid squares are H_{C2} determined from χ' , $H_{C2}^{\chi'}$, as shown in the inset of Fig. 4. The solid triangles are T_C values determined from the specific heat data T_C^{SH} using entropy-conserving construction.

Figure 6 (b) shows a reduced magnetic field h^* as a function of the reduced temperature t^* , where $h^* = H / (-dH/dT)T_C$ and $t^* = T / T_C$. The dashed-dotted and dotted lines show h^* calculated by a pair-breaking model in the clean limit and in the dirty limit,⁴¹⁻⁴³ respectively. The h^* - t^* curve obtained from the resistivity data agrees with those from the ac magnetic susceptibility and specific

heat data. The t^* dependence of h^* deviates from the calculated curve. We, therefore, determined $H_{C2}(0)$ to be 0.27 T from $\mu_0 H_{C2}^{\rho\text{-comp}}$. This value of $\mu_0 H_{C2}(0)$ is approximately one-tenth the Pauli limiting field $\mu_0 H_P$ (3.31 T), defined as $H_P = 18.4 T_C$ (kOe),^{44, 45} which indicates an absence of Pauli limiting in BaPt₂Sb₂. The Ginzburg-Landau (GL) coherent length $\xi(0)$ was determined to be 35 nm using the formula $H_{C2}(0) = \Phi_0/2\pi\xi(0)^2$, where Φ_0 is the flux quantum.⁴⁰

C. Electronic Structure

Figures 7 and 8 illustrate the band structure and the total and partial density of states (DOS) of BaPt₂Sb₂, respectively. The bands in the energy range from -0.2 to 0.0 Ry mainly consist of Sb-s states. The states in the energy range from 0.1 to 0.7 Ry mainly consist of Sb-p and Pt-d. Above 0.7 Ry, the bands originate from the Ba-d and Pt-d states. Since the band widths of Pt and Sb are broad, the correlation is deduced to be weak in BaPt₂Sb₂. Four bands cross the Fermi level E_F , as can be clearly seen in the Γ - Y line. The DOS at the Fermi level ($N(E_F)$) is 29.8 states/Ry/chemical formula unit or 2.58 states/eV/chemical formula unit. Figure 8(b) illustrates an expanded view of the partial DOS of BaPt₂Sb₂ near the Fermi level E_F . $N(E_F)$ mainly consists of Sb-p and Pt-d states and the contribution from the Pt-d states is larger in $N(E_F)$, especially that from the d states of Pt1 atoms (Pt atoms at the 4g site in Table I) are largest. The magnitudes of the contribution to $N(E_F)$ of Pt2-d, Sb2-p, and Sb1-p are approximately one half, one third, and one fifth of that from the Pt1-d states, respectively. It is worth noting that the Pt1 atom is the atom that forms the PtSb₄ tetrahedra in the Pt₂Sb₂ layers. These results suggest that the carriers mainly conduct in the Pt₂Sb₂ layers formed from the PtSb₄ tetrahedra.

As described above, the four bands cross the E_F . The bands that cross the E_F in the Γ - Y line from the Γ to Y points correspond to the 37th, 38th, 39th, and 40th bands from the bottom, respectively, which results in four sheets of FSs. Figure 9 illustrates a separate sheet of the Fermi surfaces (FSs). Two of these sheets (the FSs of the 37th and 38th bands) are hole-like and the rest are electron-like. The 37th and 38th bands form 3D FSs around the Γ point. The FSs of the 39th and 40th bands have 2D FSs with cylindrical shape along the k_z direction at the corners around the M point.

The shape of the FSs in BaPt₂Sb₂ is close to those observed in BaPd₂Sb₂²⁹ and SrPt₂As₂²²--they have two 3D FS and two 2D FSs. On the other hand, the carrier types of FSs are different between SrPt₂As₂ and the other two antimonides; SrPt₂As₂ has one hole-like FS and three electron-like FSs, while BaPt₂Sb₂ has two hole-like FSs and two electron-like FSs, as in the case of BaPd₂Sb₂.

The anisotropic shapes of the FSs are expected to be reflected in anisotropic transport properties. In order to see it, we calculated the Fermi velocity v_F^x and v_F^z assuming the angle β_{uc} in the unit cell to be 90° because the first two digits in the Fermi velocities are the same between the

crystal structure with β_{uc} of 90.00° and β_{uc} of 91.227° . Table 3 lists averaged v_F^x , v_F^z and the ratio v_F^x/v_F^z of BaPt₂Sb₂ together with the two polymorphs of BaPd₂Sb₂ and SrPt₂As₂. The values of the ratio v_F^x/v_F^z of BaPt₂Sb₂ and the CaBe₂Ge₂-type materials are clearly larger than one, which suggests that these materials have anisotropic transport properties. On the other hand, these values for the ThCr₂Si₂-type materials are almost one, suggesting isotropic transport properties. Thus, the existence of 2D FSs in BaPt₂Sb₂ and the CaBe₂Ge₂-type materials is reflected in anisotropic transport properties.

Table IV shows the superconducting critical temperatures T_C , electronic heat capacity coefficients γ_n , Debye temperatures θ_D , density of states at the Fermi level $N(E_F)$, and electron-phonon coupling constants λ of BaPt₂Sb₂, SrPt₂Sb₂,³⁰ LaPd₂Sb₂,⁴⁶ and SrPt₂As₂.^{20,22} LaPd₂Sb₂ is a recently reported superconducting material ($T_C = 1.4$ K) with the CaBe₂Ge₂-type structure. γ_n^{exp} is γ_n obtained from specific heat measurements and γ_n^{cal} is γ_n calculated using the equation: $\gamma_n^{\text{cal}} = (\pi^2/3)N(E_F)k_B^2$. The electron-phonon coupling constant λ was estimated to be 0.67 for BaPt₂Sb₂ using the relation: $\gamma_n^{\text{exp}} = (1+\lambda)\gamma_n^{\text{cal}}$. BaPt₂Sb₂ is a superconducting material with moderate coupling. The value of γ_n^{exp} of BaPt₂Sb₂ is comparable to those of SrPt₂Sb₂ and SrPt₂As₂, and is slightly larger than that of LaPd₂Sb₂. θ_D of BaPt₂Sb₂ is the smallest among the four compounds. The value of λ is comparable to that of SrPt₂As₂.

IV. CONCLUSION

This study clearly demonstrates that the 122-type antimonide, BaPt₂Sb₂, structurally related to the iron-based superconductors, shows superconductivity with a T_C of 1.8 K. BaPt₂Sb₂ crystallizes in a new-type of monoclinic variant of the CaBe₂Ge₂-type structure. The calculation shows that it has two 3D FSs and two 2D FSs, which results in anisotropic transport properties. The d-states of Pt atoms from PtSb₄ tetrahedra in the Pt₂Sb₂ layers mainly contribute to $N(E_F)$. A comparison between experimental and calculated results indicates that BaPt₂Sb₂ is a superconducting material with moderate coupling.

This study also demonstrates that unknown variants of CaBe₂Ge₂-type structure plausibly exist in the 122-type pnictides. Since it is expected that there is room for searching for superconducting materials in the 122-type antimonides, the search of antimonides with the CaBe₂Ge₂-type structure or its variants is interesting, and gives us a chance to discover new superconducting materials.

Since the calculation of the electronic structure of CaBe₂Ge₂-type iron-free pnictides shows that they have intermediate character between the ThCr₂Si₂-type iron pnictides and the ThCr₂Si₂-type iron-free pnictides, further study of the 122-type antimonides with the CaBe₂Ge₂-type structure or its variants will be important for a systematic understanding of superconductivity in the 122 pnictides.

Acknowledgements

The authors thank M. Nishio of NIMS for the EPMA, M. Takagi of NIMS for experimental support, Y. Yamada, F. Ishikawa, N. Eguchi of Niigata University for their support at the first stage in the synthesis. This work was supported in part by the Japan Society for the Promotion of Science (JSPS) through its 'Funding Program for World-Leading Innovative R&D on Science and Technology (FIRST Program)'.

References

1. Y. Kamihara, T. Watanabe, M. Hirano and H. Hosono, *J. Am. Chem. Soc.* **130**, 3296 (2008).
2. N.-L. Wang, H. Hosono and P. Dai, *Iron-Based Superconductors*. (Pan Stanford Publishing, Singapore, 2013).
3. Y. Izyumov and E. Kurmaev, *High- T_C Superconductors Based on FeAs Compounds* (Springer, Heidelberg, Dordrecht, London, New York, 2010).
4. H. Hosono, *J. Phys. Soc. Jpn.* **77**, 1 (2008).
5. D. C. Johnston, *Adv. Phys.* **59**, 803 (2010).
6. J. Paglione and R. L. Greene, *Nature Phys.* **6**, 645 (2010).
7. P. J. Hirschfeld, M. M. Korshunov and I. I. Mazin, *Rep. Prog. Phys.* **74**, 124508 (2011).
8. G. R. Stewart, *Rev. Mod. Phys.* **83**, 1589 (2011).
9. K. Ishida, Y. Nakai and H. Hosono, *J. Phys. Soc. Jpn.* **78**, 062001 (2009).
10. M. Rotter, M. Tegel and D. Johrendt, *Phys. Rev. Lett.* **101**, 107006 (2008).
11. K. Kudo, K. Iba, M. Takasuga, Y. Kitahama, J. Matsumura, M. Danura, Y. Nogami and M. Nohara, *Sci. Rep.* **3**, 1478 (2013).
12. F. Ronning, E. D. Bauer, T. Park, S. H. Baek, H. Sakai and J. D. Thompson, *Phys. Rev. B* **79**, 7, 134507 (2009).
13. T. Mine, H. Yanagi, T. Kamiya, Y. Karnihara, M. Hirano and H. Hosono, *Solid State Commun.* **147**, 111 (2008).
14. D. Hirai, T. Takayama, R. Higashinaka, H. Aruga-Katori and H. Takagi, *J. Phys. Soc. Jpn.* **78**, 4, 023706 (2009).
15. W. Jeitschko, R. Glaum and L. Boonk, *J. Solid State Chem.* **69**, 93 (1987).
16. J.-T. Han, J.-S. Zhou, J.-G. Cheng and J. B. Goodenough, *J. Am. Chem. Soc.* **132**, 908 (2010).
17. E. D. Bauer, F. Ronning, B. L. Scott and J. D. Thompson, *Phys. Rev. B* **78**, 172504 (2008).
18. D. Hirai, T. Takayama, D. Hashizume, R. Higashinaka, A. Yamamoto, A. K. Hiroko and H. Takagi, *Physica C* **470**, S296 (2010).
19. F. Ronning, N. Kurita, E. D. Bauer, B. L. Scott, T. Park, T. Klimczuk, R. Movshovich and J. D. Thompson, *J. Phys.: Condens. Matter* **20**, 342203 (2008).

20. K. Kudo, Y. Nishikubo and M. Nohara, *J. Phys. Soc. Jpn.* **79**, 123710 (2010).
21. A. Imre, A. Hellmann, G. Wenski, J. Grap, D. Johrendt and A. Mewis, *Z. Anorg. Allg. Chem.* **633**, 2037 (2007).
22. I. R. Shein and A. L. Ivanovskii, *Phys. Rev. B* **83**, 104501 (2011).
23. D. J. Singh, *Phys. Rev. B* **78**, 7, 094511 (2008).
24. C. Liu, G. D. Samolyuk, Y. Lee, N. Ni, T. Kondo, A. F. Santander-Syro, S. L. Bud'ko, J. L. McChesney, E. Rotenberg, T. Valla, A. V. Fedorov, P. C. Canfield, B. N. Harmon and A. Kaminski, *Phys. Rev. Lett.* **101**, 177005 (2008).
25. A. Subedi and D. J. Singh, *Phys. Rev. B* **78**, 132511 (2008).
26. I. R. Shein and A. L. Ivanovskii, *Phys. Rev. B* **79**, 054510 (2009).
27. I. R. Shein and A. L. Ivanovskii, *Solid State Commun.* **149**, 1860 (2009).
28. I. R. Shein and A. L. Ivanovskii, *Physica B* **405**, 3213 (2010).
29. I. Hase and T. Yanagisawa, *Physica C* **494**, 27 (2013).
30. M. Imai, S. Emura, M. Nishio, Y. Matsushita, S. Ibuka, N. Eguchi, F. Ishikawa, Y. Yamada, T. Muranaka and J. Akimitsu, *Superconductor Science & Technology* **26**, 075001 (2013).
31. R. A. Young, *The Rietveld Method*. (Oxford University Press, Oxford, 1993).
32. J. Rodriguez-Carvajal, *Physica B* **192**, 55 (1993).
33. A. Yanase, *Fortran Program For Space Group (TSPACE)* (Shokabo, Tokyo, 1995).
34. D. D. Koelling and B. N. Harmon, *J. Phys. C* **10**, 3107 (1977).
35. G. Venturini, B. Malaman and B. Roques, *J. Less-Common Metals* **146**, 271 (1989).
36. C. H. Lee, A. Iyo, H. Eisaki, H. Kito, M. T. Fernandez-Diaz, T. Ito, K. Kihou, H. Matsuhata, M. Braden and K. Yamada, *J. Phys. Soc. Jpn.* **77**, 083704 (2008).
37. D. Johrendt, H. Hosono, R. D. Hoffmann and R. Pottgen, *Z. Kristallogr* **226**, 435-446 (2011).
38. K. Kuroki, H. Usui, S. Onari, R. Arita and H. Aoki, *Phys. Rev. B* **79**, 16, 224511 (2009).
39. A. F. Khoder, *Phys. Lett. A* **94**, 378 (1983).
40. M. Tinkham, *Introduction to superconductivity*, 2nd ed. (McGraw-Hill Inc., New York, 1996).
41. E. Helfand and N. R. Werthamer, *Phys. Rev. Lett.* **13**, 686 (1964).
42. E. Helfand and Werthamer, *Phys. Rev.* **147**, 288 (1966).
43. N. Werthamer, E. Helfand and P. Hohenber, *Phys. Rev.* **147**, 295 (1966).
44. B. S. Chandrasekhar, *Appl. Phys. Lett.* **1**, 7 (1962).
45. A. M. Clogston, *Phys. Rev. Lett.* **9**, 266 (1962).
46. S. Ganesanpotti, T. Yajima, T. Tohyama, Z. Li, K. Nakano, Y. Nozaki, C. Tassel, Y. Kobayashi and H. Kageyama, *J. Alloys Compd.* **583**, 151-154 (2014).

Table I. Crystal structure of BaPt₂Sb₂. Monoclinic. Space group: C2/m (No. 12). Lattice parameters: $a = 6.70156(10)$ Å, $b = 6.75246(10)$ Å, $c = 10.47440(14)$ Å, $\alpha_{uc} = 90.000^\circ$, $\beta_{uc} = 91.2274(9)^\circ$, $\gamma_{uc} = 90.000^\circ$. $Z = 4$. $U_{iso} = 0.0057$ Å² (fixed). R-factors: $R_p = 9.86$, $R_{wp} = 12.0$, $R_e = 4.57$, $\chi^2 = 6.939$. The definitions of R_p , R_{wp} , R_e and χ^2 are described in Ref. ³¹. The figures in parentheses represent the standard deviation.

Label	Atom	Multiplicity Wyckoff position	x	y	z
Ba	Ba	4i	0.2549(6)	0.0000	0.7531(4)
Pt1	Pt	4g	0.0000	0.2823(3)	0.0000
Pt2	Pt	4i	0.2472(3)	0.0000	0.3791(2)
Sb1	Sb	4h	0.00000	0.2505(4)	0.50000
Sb2	Sb	4i	0.2276(5)	0.00000	0.1206(3)

Table 2. Interatomic distances and bond angles. The figures in parentheses represent the standard deviation.

Interatomic distances		
Intralayer		
Pt ₂ Sb ₂ layer	2.681(3) Å x 2	2.734(3) Å x2
	Sb height from the Pt square lattice	1.263(3) Å
Sb ₂ Pt ₂ layer	2.687(2) Å x2	2.702(2) Å x2
	Pt height from the Sb square lattice	1.266(2) Å
Interlayer	2.708(7) Å	
Bond angles		
PtSb ₄ tetrahedron		
Sb-Pt-Sb angle		
diagonal (α_{bond})	122.92(15)° x 2	
adjacent (β_{bond})	91.58(16)°, 102.78(12)° x 2, 113.50(19)°	
SbPt ₄ tetrahedron		
Pt-Sb-Pt angle		
diagonal (α_{bond})	123.95(12)° x 2	
adjacent (β_{bond})	102.47(12)°, 103.10(9)° x 2, 102.34(12)°	

Table III. Averaged Fermi velocity v_F^x , v_F^z and the ratio v_F^x/v_F^z for BaPt₂Sb₂ together with those of two polymorphs (CaBe₂Ge₂-type and ThCr₂Si₂-type) of BaPd₂Sb₂²⁹ and SrPt₂As₂²².

Materials	v_F^x (10^7 cm/s)	v_F^z (10^7 cm/s)	v_F^x/v_F^z
BaPt ₂ Sb ₂	4.4	2.1	2.1
The CaBe ₂ Ge ₂ type			
BaPd ₂ Sb ₂	-	-	2.9 ^a
SrPt ₂ As ₂	2.47 ^b	1.62 ^b	1.52 ^b
The ThCr ₂ Si ₂ type			
BaPd ₂ Sb ₂	-	-	0.72 ^a
SrPt ₂ As ₂	1.93 ^b	1.87 ^b	1.03 ^b

^a Ref. 29

^b Ref. 22

Table IV. Superconducting critical temperatures T_C , electronic heat capacity coefficients γ_n , Debye temperatures θ_D , calculated density of states at the Fermi level $N(E_F)$, and electron-phonon coupling constants λ of BaPt₂Sb₂, SrPt₂Sb₂³⁰, LaPd₂Sb₂⁴⁶ and SrPt₂As₂^{20, 22}. γ_n^{exp} is γ_n obtained from specific heat measurements and γ_n^{cal} is γ_n estimated by calculations. The figures in parentheses represent the standard deviation.

	T_C (K)	γ_n^{exp} (mJ/mol K ²)	θ_D (K)	$N(E_F)$ (states/eV cell)	γ_n^{cal} (mJ/mol K ²)	λ
BaPt ₂ Sb ₂	1.82	8.6(2)	146(4)	2.19	5.16	0.67
SrPt ₂ Sb ₂	2.1 ^a	9.2(1) ^a	183 ^a	-	-	-
LaPd ₂ Sb ₂	1.4 ^b	6.89 ^b	210 ^b	-	-	-
SrPt ₂ As ₂	5.2 ^c	9.72 ^c	211 ^c	2.55 ^d	6.01 ^d	0.62 ^d

^a Ref. 30

^b Ref. 46

^c Ref. 20

^d Ref. 22

Fig. 1. (Color online) Powder X-ray diffraction pattern of BaPt₂Sb₂. The red points and black line represent the observed and calculated intensities, respectively. The difference of the two intensities is shown by the blue line shifted by -5000 counts. Peak positions for BaPt₂Sb₂ and the impurity PtSb are labeled by green and purple vertical bars located at -1000 and -2000 counts, respectively.

Fig. 2. (Color online) (a) Crystal structure of BaPt₂Sb₂, (b) PtSb₄ and SbPt₄ tetrahedra that form the Pt₂Sb₂ and Sb₂Pt₂ layers, (c) view from the [010] direction, (d) view from the [111] direction, (e) deformed Pt square lattice of BaPt₂Sb₂ from the [001] direction, and (f) Pt square lattice of CaBe₂Ge₂-type BaPt₂Sb₂ from the [001] direction. Red broken lines show the Pt lattice. The blue solid lines show the unit cell. Large purple spheres, small white spheres, and small orange spheres represent Ba, Pt, and Sb atoms, respectively.

Fig. 3. (Color online) (a) Electrical resistivity as a function of temperature, (b) electrical resistivity at various constant temperatures as a function of magnetic field. The inset in Fig. 3 (a) is an expanded view of the resistivity at low temperatures ranging from 1.8 to 2.2 K. The symbols $H_{C2}^{\rho-on}$, $H_{C2}^{\rho-mid}$, $H_{C2}^{\rho-comp}$, represent the magnetic field at which ρ starts to increase from zero resistivity, the value of ρ at half of the normal resistivity value, and an extrapolation of the ρ - T curve during the transition that reaches the normal resistivity value, respectively.

Fig. 4. (Color online) Real and imaginary parts of the ac magnetic susceptibility, χ' and χ'' , measured at constant temperature below 1.44 K as a function of magnetic field amplitude $\mu_0 H$. The inset shows an expanded view of χ' measured at 0.03 K. The symbol $H_{C2}^{\chi'}$ represents a magnetic field amplitude where the diamagnetic signal disappears.

Fig. 5. (Color online) (a) Specific heat divided by the temperature C/T measured at various magnetic fields as a function of temperature squared T^2 , and (b) specific heat difference between 0 T and 0.2 T divided by temperature $[C(0\text{ T}) - C(0.2\text{ T})] / T$ as a function of the temperature.

Fig. 6. (Color online) (a) Magnetic field-temperature diagram deduced from measurements of electrical resistivity, ac magnetic susceptibility, and specific heat. The open triangle, circle and rhombus symbols indicate $T_C^{\rho-on}$, $T_C^{\rho-mid}$, and $T_C^{\rho-comp}$, as shown in Fig 3(b). The solid square and triangle symbols are H_{C2} determined from χ' and T_C determined from the specific heat data, respectively. (b) Reduced magnetic field h^* as a function of the reduced temperature t^* , where $h^* = H / (-dH/dT)T_C$ and $t^* = T / T_C$. The dashed-dotted and dotted lines show h^* calculated by a

pair-breaking model in the clean limit and in the dirty limit, respectively.

Fig. 7. Band structure of BaPt₂Sb₂.

Fig. 8. (Color online) (a) Total and partial density of states (DOS) and partial DOS of BaPt₂Sb₂. (b) Expanded view of partial DOS of BaPt₂Sb₂ near the Fermi level E_F .

Fig. 9. Fermi surfaces (FSs) of BaPt₂Sb₂. FSs of the 37th and 38th bands are hole-like and FSs of the 39th and 40th bands are electron-like.

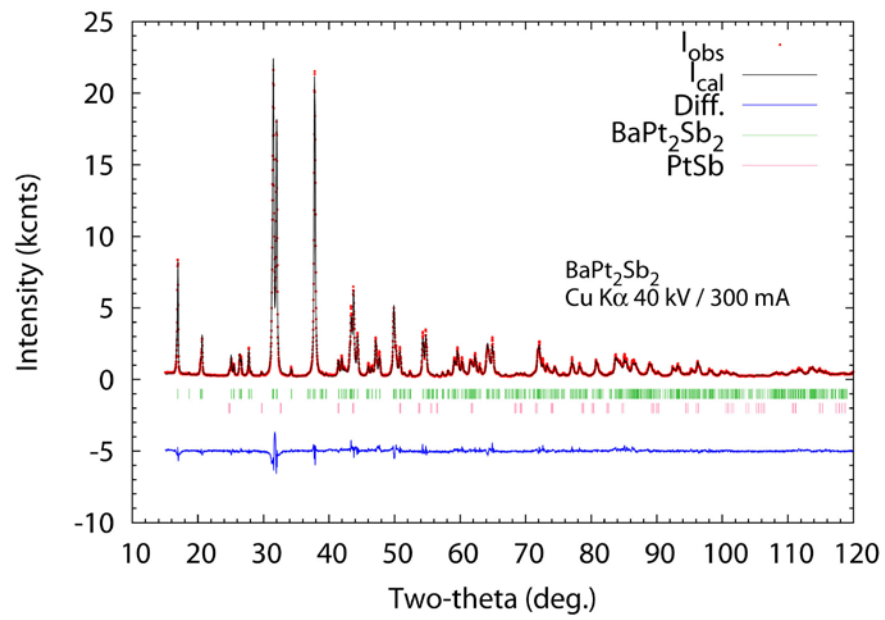


Fig. 1

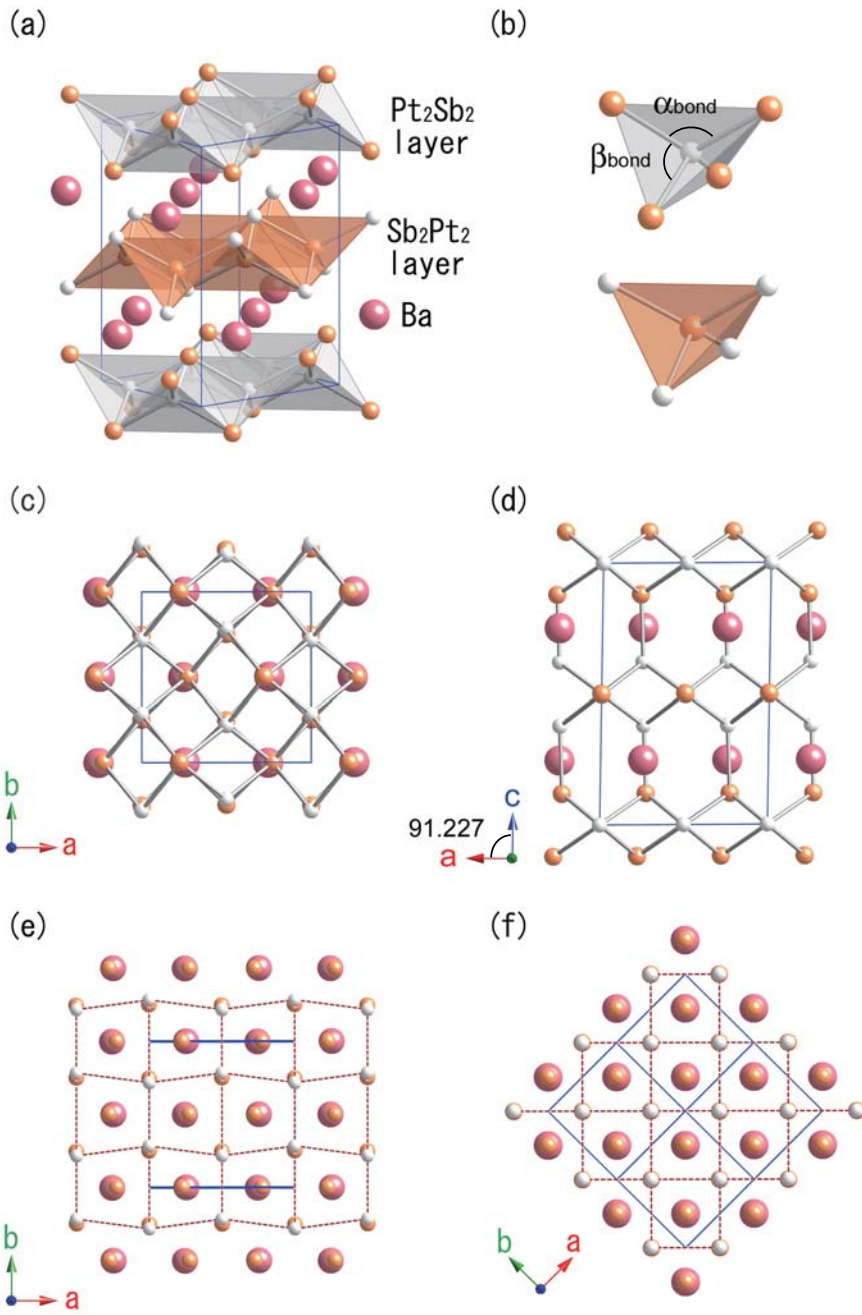


Fig. 2

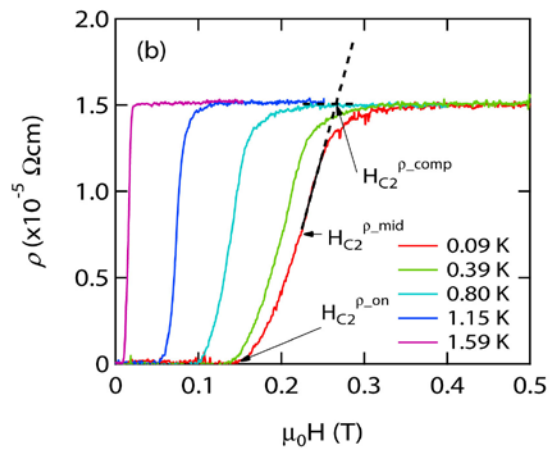
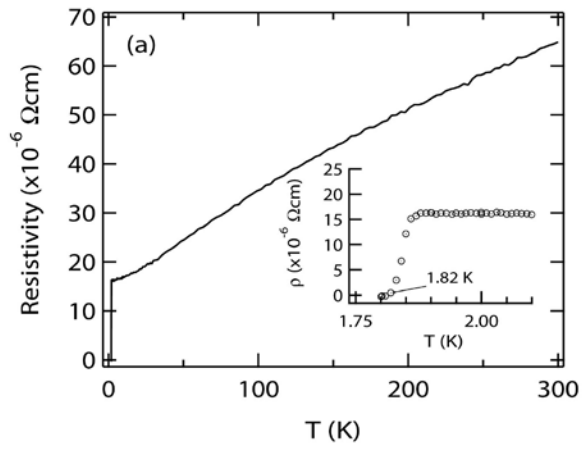


Fig. 3

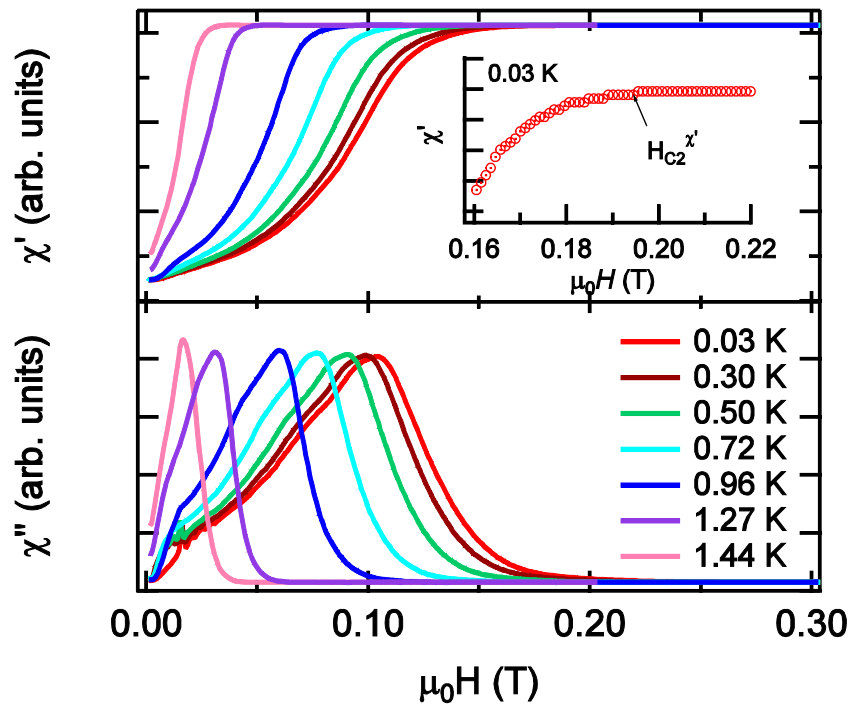


Fig. 4

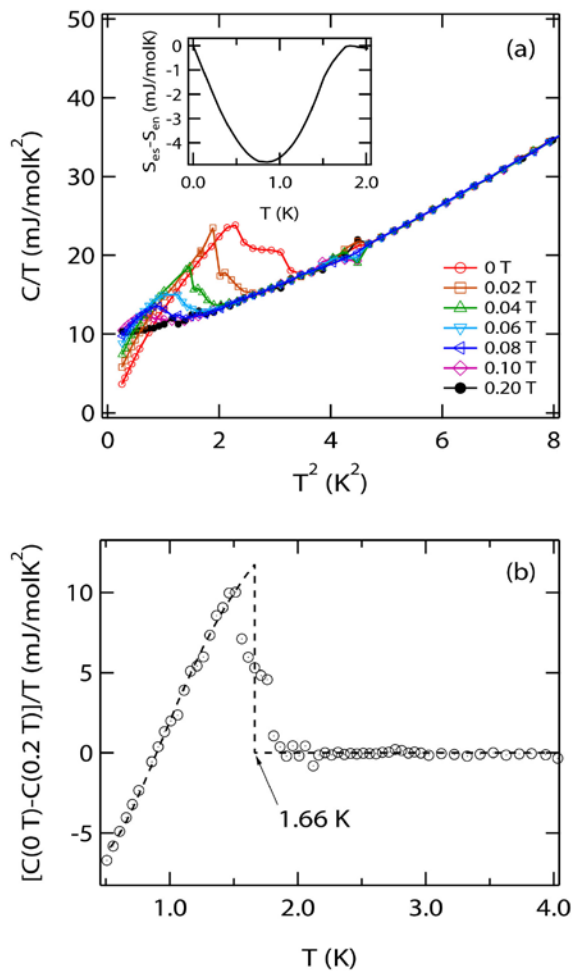


Fig. 5

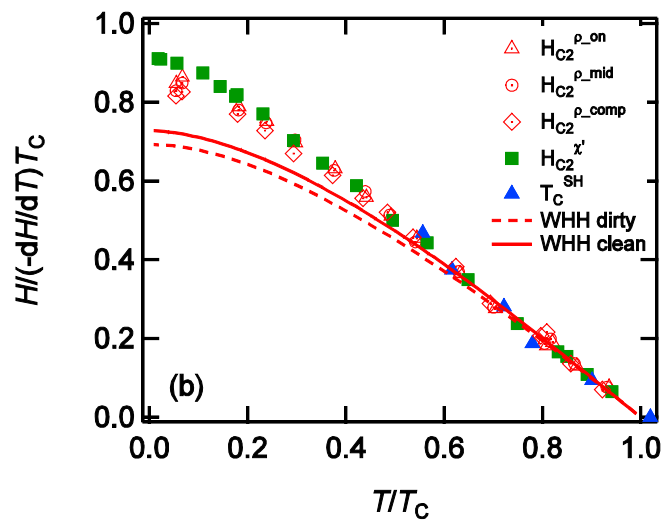
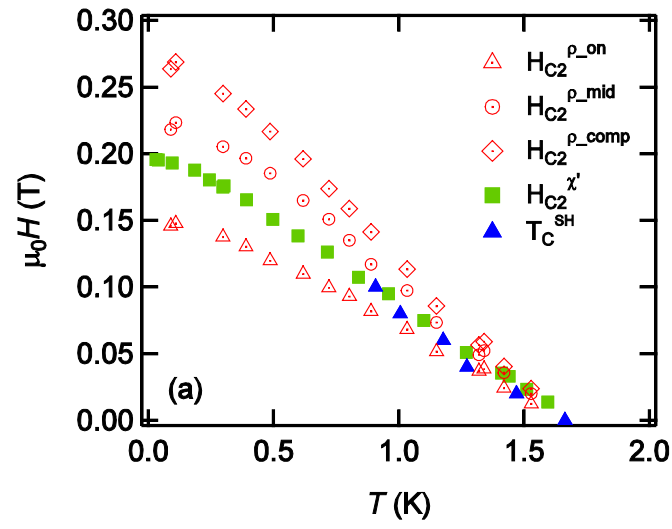


Fig. 6

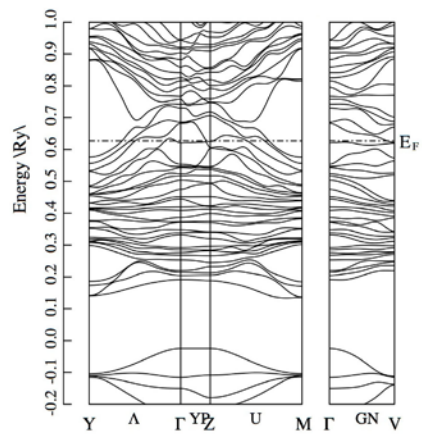


Fig. 7

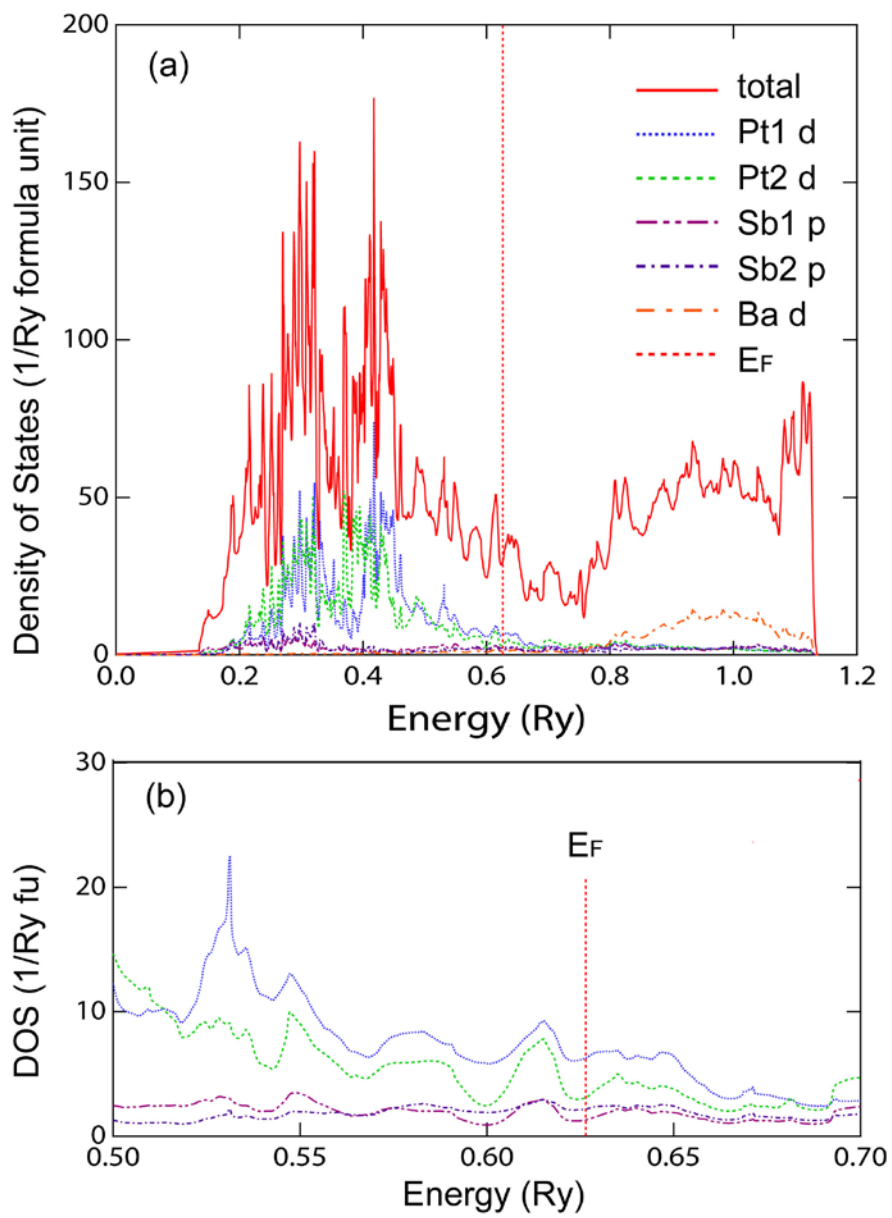
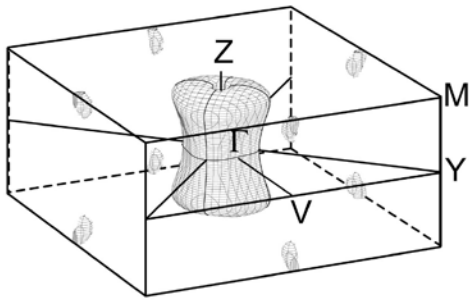
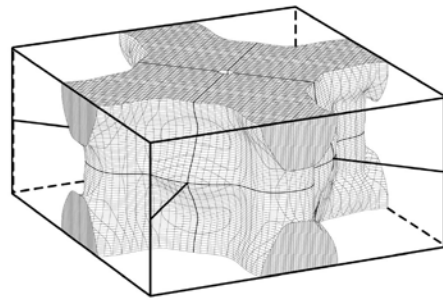


Fig. 8

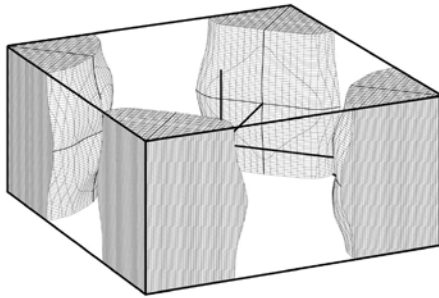
(a)



(b)



(c)



(d)

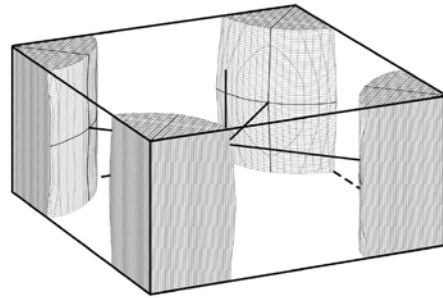


Fig. 9